

Numerical Simulation of Solidification, Homogenization, and Precipitation in an Industrial Ni-Based Superalloy



LUC ROUGIER, ALAIN JACOT, CHARLES-ANDRÉ GANDIN, DAMIEN PONSEN,
and VIRGINIE JAQUET

A comprehensive simulation approach integrating solidification, homogenization, and precipitation during aging has been used to predict the formation of γ/γ' microstructures in the AM1 nickel-based superalloy. The particle size distribution of intradendritic γ' precipitates after aging was calculated with a multicomponent diffusion model coupled with CALPHAD thermodynamics for the equilibrium at the interface. The influence of residual microsegregation after homogenization and quenching was analyzed through different initial conditions obtained from calculations of the concentration profiles in the primary γ dendritic microstructure during solidification and the homogenization heat treatment. While the global sequence of precipitation remains qualitatively the same, substantial differences in the final volume fraction of γ' precipitates were predicted between the core and the periphery of a former dendrite arm, for typical homogenization and aging conditions. To demonstrate the relevance of the developed simulation approach, the model was also used to investigate modified precipitation heat treatments. The simulations showed that relatively short heat treatments based on slow continuous cooling could potentially replace the extended isothermal heat treatments which are commonly used. Slow continuous cooling conditions can lead to similar γ' precipitates radii and volume fractions, the main differences with isothermal heat treatments lying in a narrower particle size distribution.

DOI: 10.1007/s11661-016-3694-1

© The Minerals, Metals & Materials Society and ASM International 2016

I. INTRODUCTION

NICKEL-BASED superalloys are employed to manufacture turbine blades for aeronautical applications owing to their good mechanical properties at high temperature.^[1] The microstructural features of these alloys, *i.e.*, the volume fraction and the size of the γ' precipitates embedded in the γ phase, largely determine the properties at high temperatures. For this reason, heat treatments are carried out to control the microstructure. The γ' phase forms first during solidification as a coarse interdendritic eutectic microstructure with poor mechanical properties. A solution heat treatment followed by a quench is then performed to dissolve the γ' eutectic and attenuate the composition gradients in the primary γ dendrites. The alloy is then

aged at temperatures below the γ solvus to form γ' precipitates with the desired average size and volume fraction.

The final microstructure and properties of the alloy after heat treatment are determined by the precipitation response during aging, which depends on the chemical composition of the matrix. To obtain a perfectly homogenized γ matrix of nominal composition, the material needs to be held at the solution heat treatment temperature during an extremely long time, which is not achievable in practice. Residual concentration gradients and small amounts of γ' eutectic are thus often present at the initial stage of aging. The precipitation response of the alloy during aging is therefore determined by the history of the material, starting from the solidification stage. Numerical simulation can be a very valuable approach to investigate the microstructure evolution in the material during its transformation, and potentially optimize the processing conditions in terms of properties and production cost.

Numerical simulation has been used for several decades with the aim of predicting microsegregation and precipitation in metallic alloys. Microsegregation during solidification can be quantified with analytical models such as Gulliver–Scheil and back-diffusion approaches.^[2] An important limitation of analytical models is that they cannot simulate the dissolution of interdendritic eutectics and the evolution of concentration profiles in the primary phase during the solution

LUC ROUGIER, Ph.D. Student, is with Ecole Polytechnique Fédérale de Lausanne, 1015 Lausanne, Switzerland, and also with Snecma-SAFRAN Group, 92702 Colombes, France. ALAIN JACOT, formerly Senior Scientist with Ecole Polytechnique Fédérale de Lausanne, is now Group Leader with the ESI Group, Calcom ESI SA, Route Cantonale 105, 1025 St-Sulpice, Switzerland. Contact e-mail: Alain.Jacot@esi-group.com. CHARLES-ANDRÉ GANDIN, CNRS Researcher, is with MINES ParisTech, CEMEF UMR CNRS 7635, 06904 Sophia Antipolis, France. DAMIEN PONSEN, Research Engineer, and VIRGINIE JAQUET, Research Manager, are with the Snecma-SAFRAN Group, Boulevard de Valmy - BP 31, 92702 Colombes Cedex, France.

Manuscript submitted November 16, 2015.

Article published online August 18, 2016

heat treatment. In multicomponent systems, another aspect is cross-diffusion, *i.e.*, the fact that the flux of a given chemical species is also influenced by the concentration gradients of the other species. This phenomenon is of greatest importance in Ni-based superalloys^[3] and is difficult to address with analytical approaches. Numerical models are thus generally preferred to describe microstructure evolution in superalloys. Among them, the phase field method is currently the most comprehensive approach. The complex 3D morphology of the γ dendrites and the spatial distribution of the γ' eutectic can be simulated.^[4] However, clear limitations still exist as phase-field modeling for multicomponent superalloys coupled with CALPHAD thermodynamic and kinetic databases is limited to small domains that do not simulate a representative volume encompassing several primary and secondary dendrite arms. A fine topological description of all phases, including the primary dendritic phase, the fine interdendritic multiphase eutectic microstructure plus the sub-micrometer size precipitate phase, is also not yet available. An additional difficulty is the absence of databases of temperature- and composition-dependent interfacial energies and their anisotropies for the different interfaces that form upon cooling from the liquidus down to room temperature. A review of microsegregation in nickel-based superalloys was recently conducted,^[5] revealing the state of the art on modeling. A full comprehensive integrated model of the metallurgical transformations in industrial nickel-based superalloys using a 3D phase field approach is still not accessible. With this objective, one-dimensional numerical models of diffusion remain a valid approach to predict the level of microsegregation during solidification and heat treatment, in particular when the complex chemistry of industrial alloys needs to be addressed. DICTRA^[6] and the Pseudo-Front Tracking technique (PFT)^[7-9] are examples of such approaches. This approach, with 1d cylindrical simulation of concentration profiles, has already been successfully applied for the simulation of solidification of AM1^[10] and CMSX4.^[6] In both cases, the calculated profiles are in good agreement with the measurements, which also indicates that, according to the mass conservation law, the fraction of residual eutectics predicted with these models should be reasonably accurate. It is also worth mentioning that a global modeling approach including solidification, solution heat treatment, and aging is not commonly addressed in the literature and remains a challenging task. Most recent studies consider experimental investigations on third or higher generation Ni-based superalloys, only for some of the three steps that control the microstructure of single crystals,^[11-13] while modeling should benefit the optimization of the processing route.

Simulation of precipitation can be performed by calculating the evolution of the number density and the average size of the precipitates based on nucleation, growth, and coarsening laws.^[14-16] In a more sophisticated approach, the evolution of the particle size distribution (PSD) is also tracked.^[17-23] The PSD approach is of particular interest to simulate heat treatments that are made of several cooling and aging

stages, which can lead to complex multimodal PSDs. As compared with average radius approaches, PSD models address coarsening in a more consistent way by quantifying the Gibbs–Thomson effect for each precipitate size rather than relying on assumptions such as steady-state coarsening. In PSD models, cross-diffusion can be directly taken into account by using the thermodynamic and kinetic databases to obtain the effective solute fluxes,^[22-24] reaching some success in comparison with experimental data.^[25] PSD models are based on a mean-field concept, which assumes that precipitates only interact through a matrix of average composition, neglecting the effect of the local variations of the arrangement. To remain accurate at large supersaturations, corrections are applied to the diffusion lengths, as shown by Chen *et al.*,^[24] based on the early analytical work of Aaron *et al.*^[26] Another approach was recently proposed by Guillemot and Gandin^[27] showing the importance of the choice used to estimate the far field composition seen by the growing interface while considering an exact extension to multicomponent alloys of the analytical solution proposed by Aaron *et al.*^[26]

As seen, many models are already available to address the topic of microstructure evolution during solidification and heat treatment of Ni-based superalloys. However, they seldom combine a description of the microstructure evolution during the different processing steps and the full complexity of the chemistry of industrial superalloys. The objective of this study is to present a comprehensive simulation approach which can be used to address the precipitation response of multicomponent superalloys, taking into account the aforementioned influence of solidification and complex thermodynamics. The analysis is focused on the AM1 superalloy and is largely based on numerical simulation with a PSD model of precipitation,^[22] which is coupled to an external CALPHAD computation module. A multicomponent microsegregation model^[8,9] is also used to generate the initial condition for aging, and to perform chained microsegregation and precipitation calculations. Different aging conditions, and different levels of residual segregation and volume fractions of undissolved eutectic γ' are analyzed. Finally, modified heat treatments are discussed to suggest routes for optimizations, thus demonstrating the potential of the simulation approach for the processing route of structural hardened cast alloys.^[28]

II. DESCRIPTION OF THE MODELS

Two models are applied to simulate solidification and heat treatments of the AM1 superalloy. The main focus is the study of solid-state precipitation, which is addressed with the PSD model.^[22] As this model has already been presented in details in Reference 22, only a recent modification will be introduced hereafter. For solidification/homogenization, modification of an existing framework^[8] was required in order to introduce the treatment of cross-diffusion of species. A description can be found below.

local linearization of the phase-diagram is utilized to reduce the computation time.^[8] The interface position is obtained from g_{mix}^γ . When the cell located at the left hand side of Ω_{mix} no longer contains liquid, it becomes a γ cell and is withdrawn from Ω_{mix} . Its right neighbor becomes the new interface cell.

2. Formation/dissolution of interdendritic phases and homogenization of the composition profiles in the primary solid phase

The same approach can be used to compute the formation of γ' eutectic in the interdendritic region at the end of solidification, and its growth or dissolution during further cooling and heat treatment. When the liquidus of γ' is reached, the mixture domain is considered to be made of liquid, γ and γ' . During eutectic solidification, the γ phase can form either by thickening of the already existing dendrite arms (divorced eutectics) or through the formation of new γ lamellae growing together with γ' (coupled eutectics). Considering this distinction, Eq. [2] can be reformulated as follows:

$$\bar{X}_{i,\text{mix}} = g_{\text{mix}}^L X_i^L + (g_{\text{mix}}^{\gamma_1} + g_{\text{mix}}^{\gamma_2}) X_i^{\gamma'^*} + g_{\text{mix}}^{\gamma'} X_i^{\gamma'} \quad [4]$$

where $g_{\text{mix}}^{\gamma'}$ and $X_i^{\gamma'}$ are the local volume fraction and the concentrations of γ' in the mixture region, and γ_1 and γ_2 distinguish between the γ phase deposited onto the dendrite arm and as part of the eutectic microstructure, respectively (Figure 1).

As for primary solidification, Eq. [3] and equilibrium calculations in Ω_{mix} are used to obtain the average compositions and the phase fractions. The position of the γ/mix interface is determined by the evolution of $g_{\text{mix}}^{\gamma_1}$ in Ω_{mix} . As thermodynamic calculations only provide the variation of the total proportion of γ in Ω_{mix} , $\Delta(g_{\text{mix}}^{\gamma_1}) + \Delta(g_{\text{mix}}^{\gamma_2})$, a supplementary condition is required to express the localization of γ :

$$P_{\text{eut}} = \frac{\Delta(g_{\text{mix}}^{\gamma_1})}{\Delta(g_{\text{mix}}^{\gamma_1}) + \Delta(g_{\text{mix}}^{\gamma_2})} \quad [5]$$

where $\Delta(g_{\text{mix}}^{\gamma'})$ is the variation of $g_{\text{mix}}^{\gamma'}$ during the time-step, and P_{eut} is a parameter of the model that takes a chosen value between 0 (purely coupled eutectic) and 1 (purely divorced eutectic).

B. Precipitation: The Particle Size Distribution Model

For the simulation of precipitation, a model based on the evolution of the PSD is used.^[22] It consists of tracking the evolution over time of the PSD by computing, for each size class, average quantities such as the precipitate radius, the number density, and the interface concentration. A Lagrangian approach is used, which means that each class represents a group of precipitates nucleated during the same time interval, and the density of precipitates in a given class is fixed, while the representative radius of the class varies over time. The growth and dissolution of the precipitates in the different classes are calculated from the solute fluxes at the γ/γ' interface. Cross-diffusion is taken into account, using a dynamic calculation of the diffusion matrix

based on the current temperature and average compositions of γ . This is achieved through direct coupling with thermodynamic and kinetics databases, Ni20^[29] and MobNi2,^[30] respectively. The model and details on the computation procedure are presented in Reference 22. For the present study, the model was modified to account for the high volume fractions of precipitates in industrial Ni-based superalloys. The solute fluxes are corrected according to the expression formulated by Marqsee and Ross^[31] as

$$J_{i,k}^{\text{corr}} = J_{i,k} \cdot \left(1 + R_k \cdot \sqrt{4\pi n_{\text{tot}} \bar{R}_N} \right) \quad [6]$$

where $J_{i,k}$ is the flux of solute element i calculated for the size class k , R_k is the radius of the precipitates of class k , and n_{tot} and \bar{R}_N are, respectively, the total precipitates density and the number-averaged radius.

III. RESULTS AND DISCUSSION

A. Solidification and Homogenization

Simulations with the PFT model have been carried out for the industrial AM1 superalloy in order to describe the formation of interdendritic γ' eutectic formed during the late stages of solidification, and its dissolution during the homogenization/solution heat treatments. The effect of the characteristic microstructure length was investigated through a series of one-dimensional cylindrical calculations with different domain sizes: $\lambda_d = 20, 50, 100,$ and $250 \mu\text{m}$. The domain size of $\lambda_d = 20 \mu\text{m}$ corresponds to half of the minimal value for the secondary dendrite arm spacing reported in References 32 and 33, while $250 \mu\text{m}$ is close to the maximal values for the primary interdendritic spacing.

The nominal alloy composition, X^0 , used for the calculations is summarized in Table I. The thermal history used in the simulation is composed of two main stages. The alloy is first solidified using a constant cooling rate of -0.2 K/s , down to 873 K ($600 \text{ }^\circ\text{C}$), before undergoing a solution/homogenization heat treatment at 1573 K ($1300 \text{ }^\circ\text{C}$) during 3 hours (10800 seconds).

Figure 2 shows the evolution of the volume fraction, g , of liquid, γ and γ' with temperature, T , during solidification. The temperatures at which the last liquid disappears, T_{sol} , are summarized in Table II. As expected, an increase of λ_d , which is associated with a decrease of the Fourier number, translates into a decrease of T_{sol} , due to a reduced effect of back-diffusion. The temperature of formation of γ' , $T^{\gamma'}$, is however almost independent of λ_d , as shown in Table II.

Figure 3 shows the normalized concentration profiles for two solute elements in the as-cast state and after the dissolution/homogenization heat treatment. Al has been selected for its important role in the γ' chemistry, while W is the slowest diffusing element. The segregation indices are shown in Figure 4 for all solute chemical species. They are defined from the minimum and maximum concentrations in the γ region:

Table I. Nominal Composition of the AM1 Superalloy, X^0 , Used for the Calculations (in At. Pct)

Ni	Al	Co	Cr	Mo	Ta	Ti	W	X^0
Balance	11.82	6.64	8.68	1.25	2.66	1.51	1.80	X^0

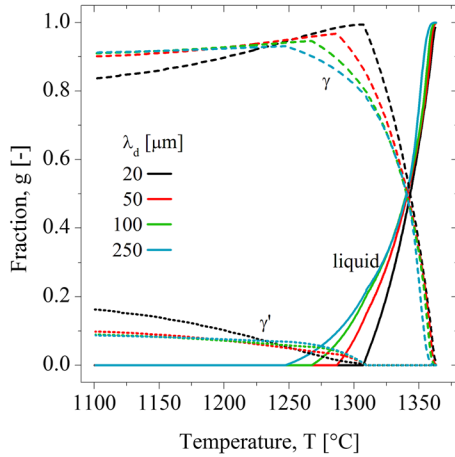


Fig. 2—Calculated volume fractions of (dashed) γ , (dotted) γ' and (plain) liquid, vs temperature during solidification of an AM1 superalloy for various values of the half of the dendrite arm spacing, λ_d .

Table II. Temperatures for the End of Solidification, T_{sol} , and the Start of γ' Precipitation, T' , Obtained with the PFT Model for Different Domain Sizes, λ_d

λ_d (μm)	T_{sol} [K (°C)]	T' [K (°C)]
20	1580.35 (1307.2)	1584.55 (1311.4)
50	1559.95 (1286.8)	1582.95 (1309.8)
100	1540.65 (1267.5)	1582.65 (1309.5)
250	1520.25 (1247.1)	1582.55 (1309.4)

$$\chi_i = \text{sign}(X_{i,k^*-1} - X_{i,1}) \frac{\max_k(X_{i,k}) - \min_k(X_{i,k})}{X_i^0} \quad [7]$$

where X_{i,k^*-1} is the concentration of solute i in the γ cell just behind the interface, and \min_k and \max_k are the minimum and maximum functions applied to all γ cells. The index k of the γ cells comprises between 1 and k^*-1 .

In the as-cast state shown in Figures 3(a) and (b), most of the composition profiles exhibit an extremum in the vicinity of the dendrite periphery. For Al, a maximum of X_{Al} is observed near $x/\lambda_d = 0.85$ (Figure 3a), while a minimum is seen for X_W at about $x/\lambda_d = 0.9$ (Figure 4b). The amplitude of these extrema increases with λ_d . For a value as small as 20 μm , no extrema are observed.

The development of extrema in the concentration profile can be explained by consideration of back diffusion and the evolution of the concentrations at the boundary of the primary γ phase. This is a common feature in the as-cast state of metallic alloys.^[34] For Al, the partition coefficient is smaller than 1 and the liquid is progressively enriched as solidification proceeds, leading

to a typical composition profile with a positive slope in the primary dendritic γ solid phase when solidification is completed, *i.e.*, at the solidus T_{sol} given in Table II. When the solidified alloy is further cooled down, the composition of Al at the boundary of the primary dendritic γ phase decreases, as it follows the γ/γ' solvus and the solubility of Al in γ decreases. At large Fourier number ($\lambda_d = 20 \mu\text{m}$), the decrease of $X_{Al}^{*\prime}$ affects the entire γ phase (the situation is close to full mixing in the solid phase), and no extremum is formed. However, for coarser dendritic microstructures, the modified conditions at the γ/γ' interface only affect the periphery of the primary γ phase, while its core still exhibits a profile with a positive slope inherited from the solidification stage. A similar situation is obtained with W. It is however fully reversed due to a partition coefficient larger than 1, and an increase of the solubility of W in γ upon cooling. The extremum is also located closer to the boundary with the γ' eutectic microstructure due to shorter diffusion lengths.

As expected, the amplitude of segregation in the as-cast state generally increases with λ_d (Figure 4(a)). The main exception to this rule is the case of W, for which a decrease of χ is observed when λ_d increases. This is correlated with the operating point of the interface. Figures 3(a) and (b) show the Al and W concentrations at the interface in γ for different λ_d . While this concentration is almost independent of λ_d for Al (except for some differences with $\lambda_d = 20 \mu\text{m}$), it strongly varies for W. The W concentration in γ at the interface is found to increase with λ_d , leading to a decrease of the interval between the extrema, $\max_k(X_{W,k}) - \min_k(X_{W,k})$. It seems thus, that in the particular case of W, the segregation index is not much affected by W diffusion on the scale of λ_d during the solidification time, which remains limited in all cases. Instead, the segregation index of W is largely affected by differences of the interface operating point, which strongly depends on λ_d . In other words, the decrease of χ_W for increasing λ_d is understood as the result of the diffusion of the other species, which leads to substantial variations of the operating points rather than diffusion of W itself.

Figure 5 shows the evolution of the γ' fraction during the isothermal heat treatment at 1573 K (1300 °C). The initial volume fraction of γ' can be read from the position of the sharp composition change in Figures 3(a) and (b). It increases with the size of the dendritic primary γ phase. After a typical heat treatment of 3 hours, γ' is totally dissolved for $\lambda_d = 20$ and 50 μm , while remaining volume fractions of about 1 and 3.3 pct are still observed for $\lambda_d = 100$ and 250 μm , respectively. Considering the typical spacings of industrial samples (about 300 μm corresponding to $\lambda_d = 150 \mu\text{m}$ ^[33]), these results can be considered as in agreement with industrial practice,

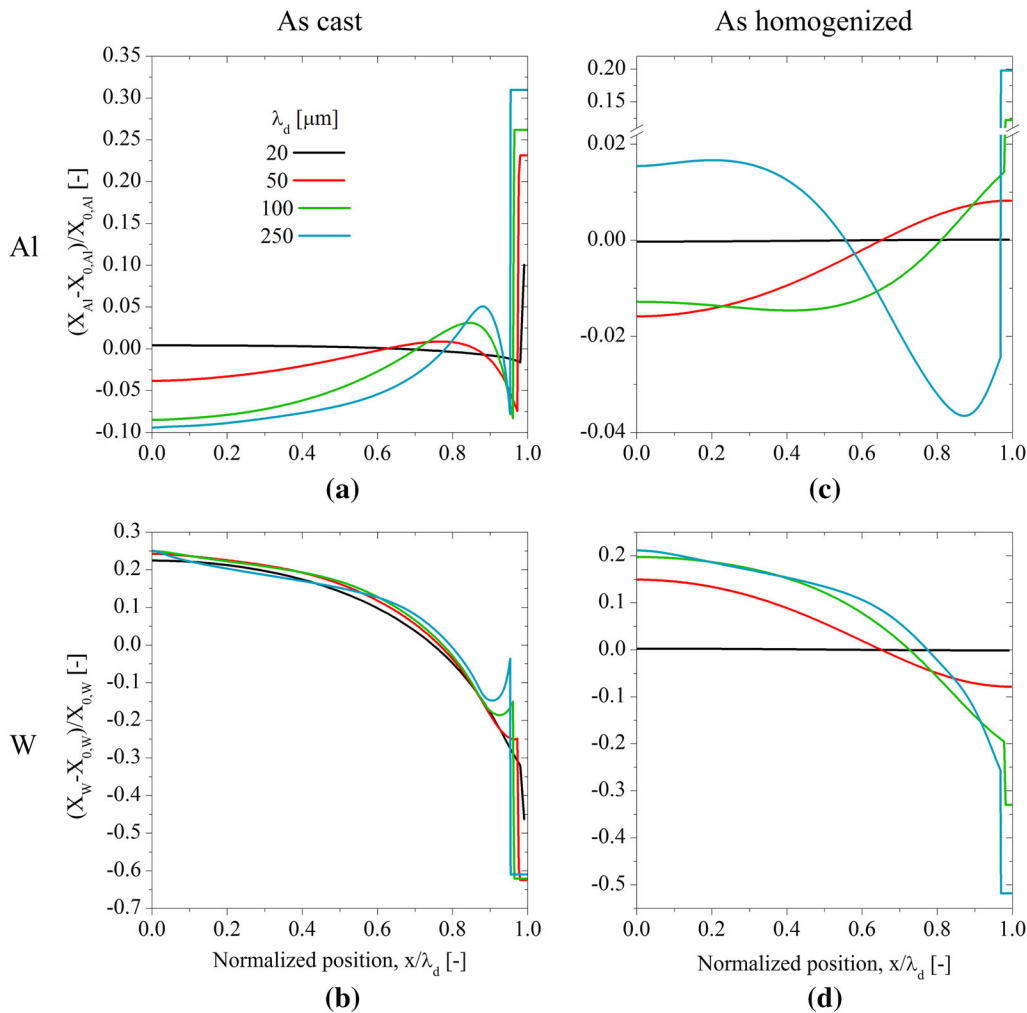


Fig. 3—Normalized composition profiles of Al and W vs the normalized position in the dendrite arm (a, b) for the as-cast state and (c, d) after the solution heat treatment.

knowing also that the present heat treatment conditions were optimized to obtain full dissolution in minimum time at 1573 K (1300 °C). As shown in Figure 5, the dissolution rate $dg\gamma'/dt$ is smaller when λ_d is high, which is due to a smaller volume density of interfaces and the time needed to diffuse the solute species to the core of the γ matrix phase.

The segregation indices for all the solute elements after the heat treatment are shown in Figure 4(b). The segregation indices are obviously smaller after heat treatment. More interesting to notice is that substantially lower concentration gradients are obtained when the dissolution of interdendritic γ' is complete (Figures 3(c) and (d)). As long as γ' is present in the microstructure, the concentrations at the boundary of the γ phase are prescribed from the local equilibrium with γ' , and gradients are difficult to eliminate. Analyses of the evolution of the segregation indices vs. time have shown that χ_i indeed decrease considerably faster once γ' has disappeared. This indicates that the complete dissolution of γ' is an important threshold to be reached during heat treatment, not only for the detrimental role that this eutectic phase may have in terms of mechanical

properties, but also in terms of homogeneity of the γ matrix prior to the aging heat treatment.

Table III summarizes the local γ concentrations, at $X = 0$ and 97.8 μm , after the standard homogenization heat treatments considering a domain size of $\lambda_d = 100 \mu\text{m}$. These compositions can also be read for Al and W at the periphery of the profiles in the γ phase displayed in Figures 3(c) and (d), respectively. They will serve as initial conditions for the precipitation calculations discussed in the next section.

B. Precipitation

1. Validation of the PSD model

In order to calibrate the simulation approach for precipitation in the AM1 superalloy, the PSD model was first used to perform comparisons with experimental data collected on a series of specimens that underwent a simplified heat treatment. After an initial cooling at -5 K/s from 1573 K (1300 °C), AM1 samples were aged during 2×10^5 seconds at 1373 K (1100 °C) and 1.5×10^4 seconds at 1483 K (1210 °C). Scanning electron microscopy characterizations were then carried out

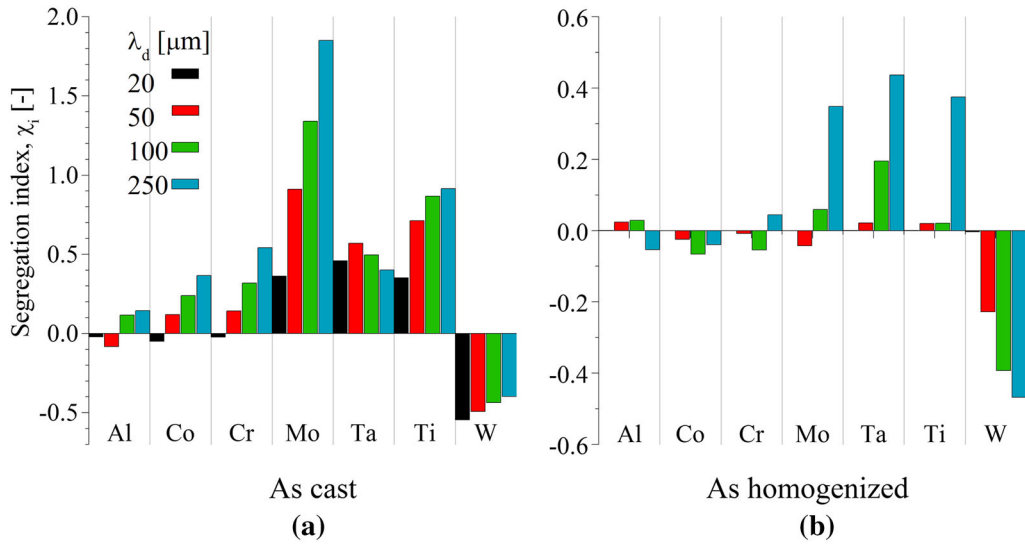


Fig. 4—Calculated segregation indices in AM1, (a) in the as-cast state, and (b) after the solution heat treatment.

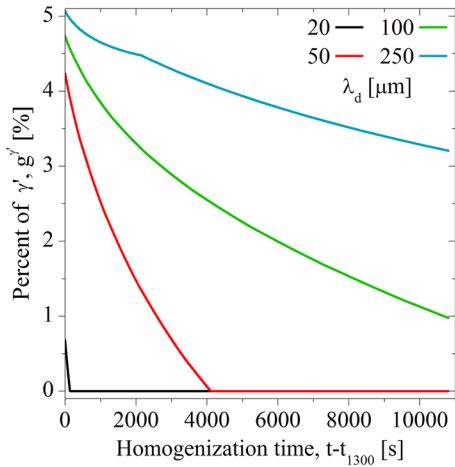


Fig. 5—Time evolution of the volume fraction of interdendritic γ' during isothermal holding at 1573 K (1300 °C).

to determine the average radius of the γ' precipitates. As the observations were focused on the dendrite core,^[35] the simulations were not performed with the nominal chemistry of AM1. Instead, the concentration calculated with the PFT model at $x = 0 \mu\text{m}$ after the standard solution/homogenization heat treatment was used as an initial condition for the supersaturated γ matrix (Table III).

The interfacial energy, $\sigma^{\gamma/\gamma'}$, was assumed to vary linearly with the temperature according to the law $\sigma^{\gamma/\gamma'}(T) = \sigma_0^{\gamma/\gamma'} + (d\sigma^{\gamma/\gamma'}/dT)(T - T_0)$ where $\sigma_0^{\gamma/\gamma'} = \sigma^{\gamma/\gamma'}(T_0)$ is a value adjusted at reference temperature T_0 and $(d\sigma^{\gamma/\gamma'}/dT)$ is a sensitivity coefficient taken from coarsening observations in the Nimonic 115 nickel-based superalloy.^[36] The values $(T_0, \sigma_0^{\gamma/\gamma'})$ were adjusted to reproduce the precipitate size evolution in AM1 reported by Grosdidier *et al.* for isothermal holdings.^[37] Table IV summarizes the chosen values.

Figure 6 shows the evolution of the volume average radius, \bar{R}_V , with time, for both simulations (lines) and measurements (symbols). A reasonable agreement is observed, especially at 1373 K (1100 °C). For long aging times, a $\bar{R}_V \sim t^{1/3}$ dependence is reached in the PSD simulations, which is characteristic of a steady state coarsening regime.

The results show good agreement between the experiments and the simulation, although the model slightly underestimates the radius of the precipitates at 1483 K (1210 °C). Potential reasons for this discrepancy are the simplifying hypotheses of the PSD model and the limits of accuracy of the thermodynamic and kinetic databases. However, as compared with previously published data, the model shows a substantially better accuracy.^[23] Using the dendrite core composition rather than the nominal chemistry, a temperature-dependent interfacial energy and corrections for high volume fractions of precipitates are at the origin of this improvement.

2. Simulation of precipitation for the standard heat treatment and the nominal AM1 composition

Precipitation of γ' in AM1 has been simulated with the nominal composition presented in Table I, and a heat treatment close to standard industrial aging practice. The temperature cycle is schematized in Figure 7(STD). The heat treatment consisted of an isothermal holding at 1373 K (1100 °C) during 5 hours, followed by 16 hours at 1143 K (870 °C). The initial temperature was 1573 K (1300 °C), and the cooling rate was -5 K/s .^[38] At the end of aging, the temperature was further decreased at -5 K/s . The calculation was stopped at 973 K (700 °C), assuming microstructure changes then become negligible, which is confirmed by the results of the simulations presented hereafter. Validation of the latter assumption is given elsewhere.^[39] All properties (thermodynamic and kinetic database, interfacial energy and its dependence with respect to temperature) were the same as in the calculations presented in the previous section.

Table III. Calculated Local Compositions in the Dendrite Arm After 3 h (10800 s) at 1573 K (1300 °C), With $\lambda_d = 100 \mu\text{m}$

Position	Ni	Al	Co	Cr	Mo	Ta	Ti	W	
0 μm	balance	11.67	6.87	8.98	1.21	2.33	1.50	2.16	X^{0-}
97.8 μm	balance	11.99	6.44	8.51	1.23	2.84	1.53	1.45	X^{0+}

Table IV. Interfacial Energy Parameters Used in the PSD Simulations

Reference Interfacial Energy, $\sigma_0^{\gamma/\gamma'}$ (mJ m^{-2})	30
Reference temperature, T_0	1373 K (1100 °C)
Sensitivity coefficient, $(d\sigma^{\gamma/\gamma'}/dT)$ ($\text{mJ m}^{-2} \text{K}^{-1}$)	-3.6×10^{-2}

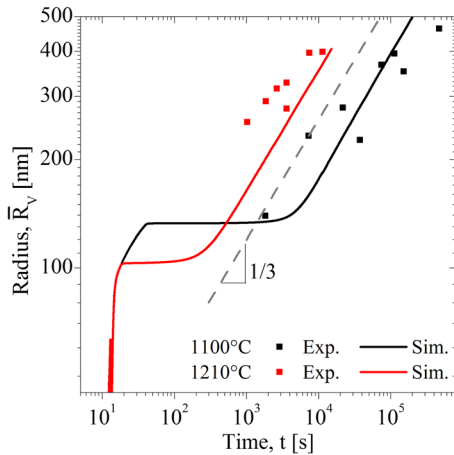


Fig. 6—Experimental (symbols) and calculated (lines) volume-averaged precipitate radius vs time, at 1373 K and 1483 K (1100 °C and 1210 °C).

Figure 8 shows the evolution of the number-averaged and volume-averaged radii, the total number density and the volume fraction of precipitates, as well as the temperature history (dashed gray curve). During cooling from 1573 K to 1373 K (1100 °C to 1300 °C), a first population of precipitates nucleates and grows rapidly. When the 1373 K (1100 °C) plateau is reached, the average radius of the precipitates is about 180 nm and the volume fraction is close to the equilibrium value ($g^{\gamma',\text{eq}} = 0.47$, Figure 8(c)). These quantities do not significantly evolve during the isothermal holding at 1373 K (1100 °C), except for an increase of the volume-averaged radius and a decrease of the number density at aging times larger than 4000 seconds (Figures 8(a) and (b)). This evolution corresponds to the onset of coarsening, which needs ‘incubation’ before becoming effective. This incubation is associated with a transient regime which involves a rearrangement of the PSD. The main mechanism operating during the isothermal hold at 1373 K (1100 °C) is thus coarsening, since growth is comparatively much faster and mostly takes place during cooling, *i.e.*, before 40 seconds. Note that the time for the onset of coarsening is in line with the previous simulation at 1373 K (1100 °C) shown in Figure 6.

Figure 9 shows the precipitate size distributions at different steps during the standard heat treatment (STD). The symbols t^S and t^E correspond to the times at the beginning and end of the corresponding temperature plateaus. These values are reported in Figure 7. After the initial cooling from 1573 K to 1373 K (1300 °C to 1100 °C), the distribution is narrow, with a single peak near 180 nm. During the first temperature plateau at 1373 K (1100 °C), the distribution remains monomodal and broadens, which is consistent with the aforementioned initial transient regime of coarsening.

During cooling from 1373 K to 1143 K (1100 °C to 870 °C), the supersaturation increases, and nucleation is resumed. This translates into an increase of the density of precipitates (Figure 8(b)), a corresponding decrease of the number-averaged radius (Figure 8(a)) and the appearance of a second population in the PSD (Figure 9 at t_{870}^S). However, the volume fraction of γ' is not significantly influenced by the nucleation of new precipitates, due to their small size. Coarsening takes place during the isothermal holding at 1143 K (870 °C). Due to the presence of a bimodal distribution, the classical steady state coarsening regime, which would be characterized by $n_{\text{tot}} \sim t^{-1}$ and $\bar{R}_V \sim t^{1/3}$, is not reached. Instead, we observe a rapid decay of n_{tot} and an increase of \bar{R}_V followed by a regime during which these quantities are nearly constant (Figures 8(a) and (b)). The variations of n_{tot} and \bar{R}_V are associated with a rearrangement of the PSD, mostly on its left hand side. The smallest precipitates disappear, while the largest particles of the second population grow. At t_{870}^E , the peak associated with the second population is totally smeared out and the size distribution is again monomodal and slightly shifted towards larger sizes compared to t_{1100}^E . The fact that \bar{R}_V and n_{tot} are nearly constant indicates that the distribution has not finished to rearrange and the ‘incubation’ time required for steady state coarsening to establish is not over.

During the final cooling, from 1143 K to 973 K (870 °C to 700 °C), a third nucleation burst is observed and the density of small precipitates dramatically increases (Figures 8(b) and 9 at t_{700}^E). Due to the very small radii of the new precipitates and their high number density, the number-averaged radius strongly decreases, while the volume-averaged radius remains almost constant. The volume fraction of γ' does not evolve

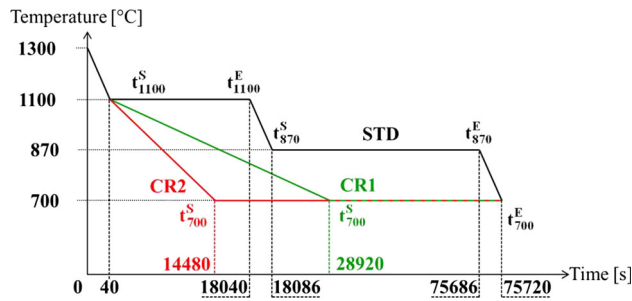


Fig. 7—Schematic representation of the prescribed CR temperature for the standard (STD) and modified heat treatments (CR1 and CR2).

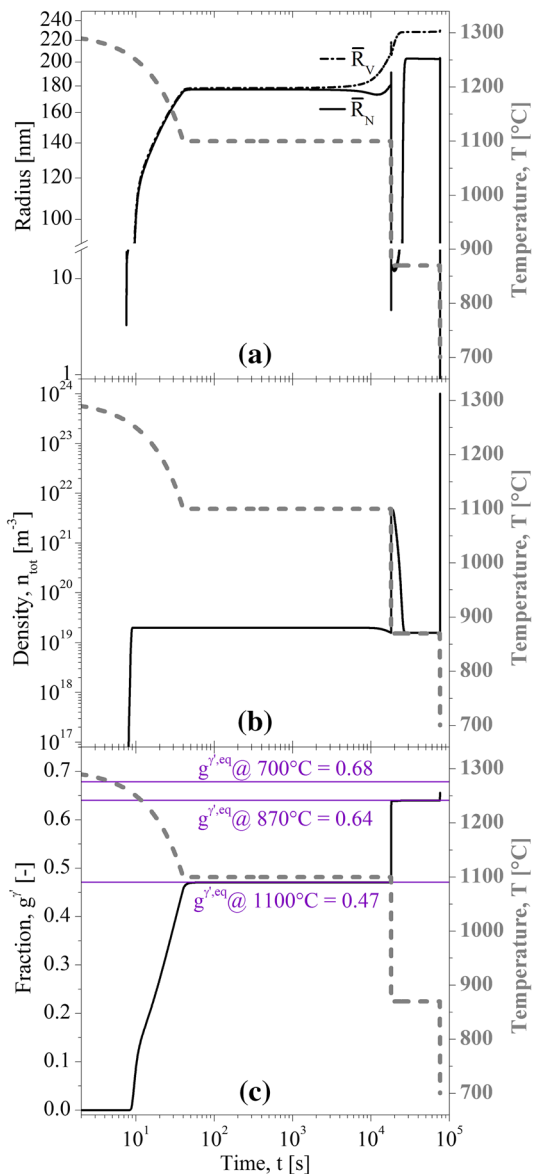


Fig. 8—Calculated time evolutions of (a) the volume average radius, \bar{R}_V , and the number average radius, \bar{R}_N , (b) the total number density and (c) the volume fraction of γ' precipitates for alloy AM1 at (Table I) nominal composition X^0 . The equilibrium values of the volume fractions of γ' at 1373 K, 1143 K, and 973 K (1100 °C, 870 °C, and 700 °C) are given in (c) with horizontal lines.

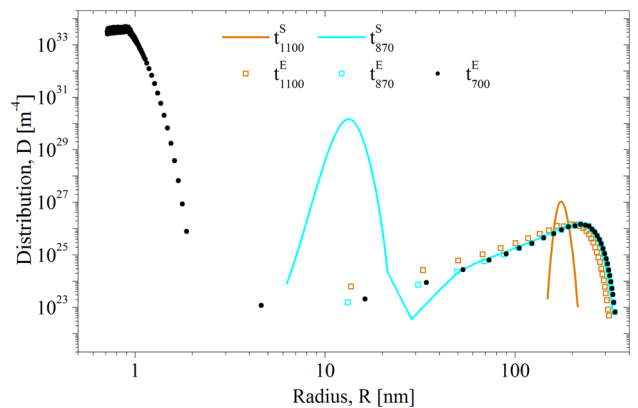


Fig. 9—Precipitate size distributions calculated at different times of the standard heat treatment for the nominal composition X^0 (Table I).

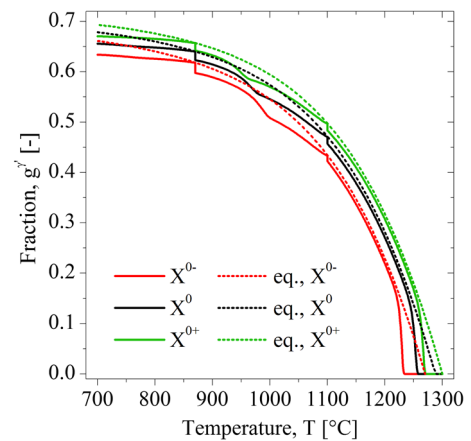


Fig. 10—Variations of the (continuous lines) calculated and (dotted lines) equilibrium volume fraction of γ' with temperature, for the three compositions X^{0-} , X^0 and X^{0+} given in Tables I and III (respectively, the dendrite core composition, the nominal composition and the dendrite periphery composition at the end of the homogenization heat treatment).

significantly during cooling from 1143 K (870 °C), due to the rapid decay of the growth kinetics as the temperature decreases. We shall later confirm this observation.

3. Influence of residual microsegregation on precipitation

Chained PFT-PSD simulations have been carried out to assess the effect of residual microsegregation on the kinetics of phase transformation during the standard aging heat treatment. The local compositions in the dendrite arm calculated with the PFT model after the solidification and standard solutionizing/homogenization heat treatments were used as initial matrix compositions for PSD calculations. The concentrations presented in Table III at positions 0 and 97.8 μm were used for two distinct PSD simulations, considering that they are representative of conditions in the core and at the periphery of a dendrite arm. These two precipitation calculations are referred hereafter as X^{0-} (core) and X^{0+}

(periphery), and are compared with an additional calculation (X^0) carried out with the nominal composition of AM1 given in Table I.

Figure 10 shows the evolution of the calculated volume fractions of γ' vs temperature for the three conditions. The equilibrium values are also represented (dotted lines). At the dendrite periphery (X^{0+}), precipitation starts at higher temperatures than for the nominal chemistry (X^0), which is explained by higher concentrations of γ' forming elements, and thus a higher solvus temperature. Oppositely, with X^{0-} , the γ phase is depleted in γ' former and precipitation starts at a lower temperature than X^0 . Because similar shifts are observed on the equilibrium volume fractions, the effect seems to be largely due to thermodynamics.

The difference between the core and the periphery of the dendrite arm is expected to be slightly less pronounced in reality due to the long distance solute exchanges which tend to homogenize the matrix composition as precipitation proceeds. This phenomenon could be addressed by coupling the PFT and PSD models, as it was done for Al alloys.^[7] Such coupling was not undertaken here due to the computational cost associated with the complex chemistry of AM1.

4. Modified heat treatments

The PSD model was also used to investigate different precipitation heat treatments. The objective was to compare continuous cooling conditions with more classical heat treatments based on isothermal temperatures plateaus such as the simplified STD described previously. The latter was compared with two continuous cooling heat treatments characterized by a slow cooling rate, CR1 = -0.014 K/s, and a faster cooling rate, CR2 = -0.028 K/s. The details of the temperature histories are presented in Figure 7. Precipitation below 973 K (700 °C) was not considered in the simulations. For the sake of comparisons with the STD, calculations CR1 and CR2 were however extended by isothermal holding at 973 K (700 °C) in order to reach the same total duration as in STD (75720 seconds). The calculations were performed with the nominal composition of AM1 given in Table I and the same parameters as in the previous simulations.

Figure 11 shows the evolution of (a) the averaged radius, (b) the total density and (c) the volume fraction of the γ' precipitates for the three heat treatments. For all heat treatments, nucleation and growth of a first population of precipitates are observed during the first cooling from 1573 K to 1373 K (1300 °C to 1100 °C). When cooling is not interrupted at 1373 K (1100 °C) (CR1 and CR2), the average radius of the precipitates keeps increasing, due to continuous resaturation of the γ matrix. As opposed to the STD heat treatment, no significant increase of n_{tot} is obtained with CR1 and CR2, indicating that nucleation essentially takes place during the initial cooling from 1573 K to 1373 K (1300 °C to 1100 °C). The precipitate size distribution shown in Figure 12 confirms that the first population of precipitates grows between t_{1100}^S and t_{700}^S for both CR1 and CR2, which translates by a shift of the peak to

larger sizes. However, with CR2, a second population of very small precipitates, having radii lower than 5 nm, does appear during cooling. As already seen with the STD heat treatment, due to relatively rapid cooling, the growth of the first population of precipitates is not fast enough to absorb the increase of supersaturation associated with the temperature change, and hence the nucleation of new particles. The calculations indicate that the critical cooling rate to avoid the nucleation of a second population of precipitates is between CR1 (0.014 K/s) and CR2 (0.028 K/s).

As shown on Figure 11(a), the final values of \bar{R}_V are similar for the three heat treatments. Furthermore, with the heat treatments CR1 and CR2, the final radii and volume fraction of γ' are almost reached at the end of the cooling ramps. More precisely, γ' volume fractions

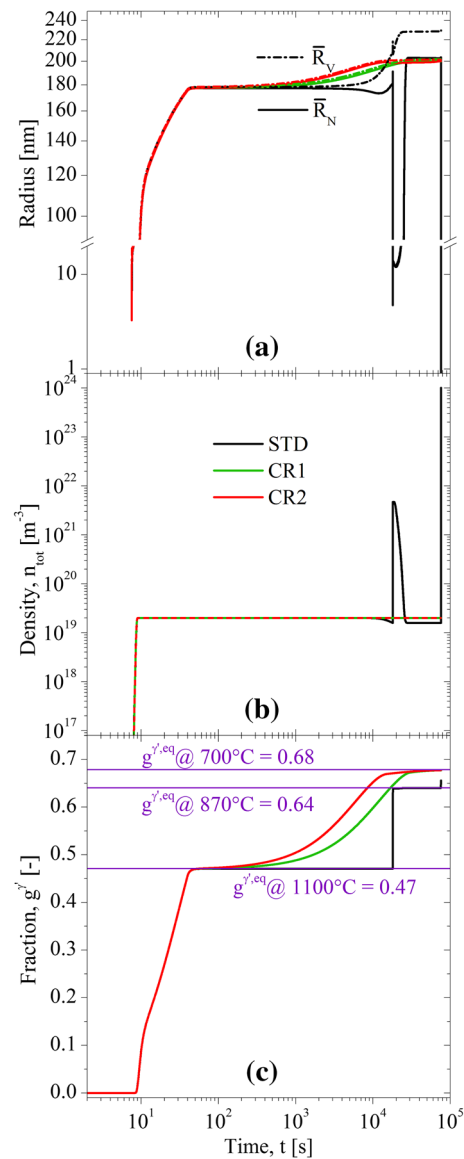


Fig. 11—Time evolution of (a) the average radius, (b) the total number density and (c) the volume fraction of γ' precipitates calculated for the STD, CR1 and CR2 heat treatments.

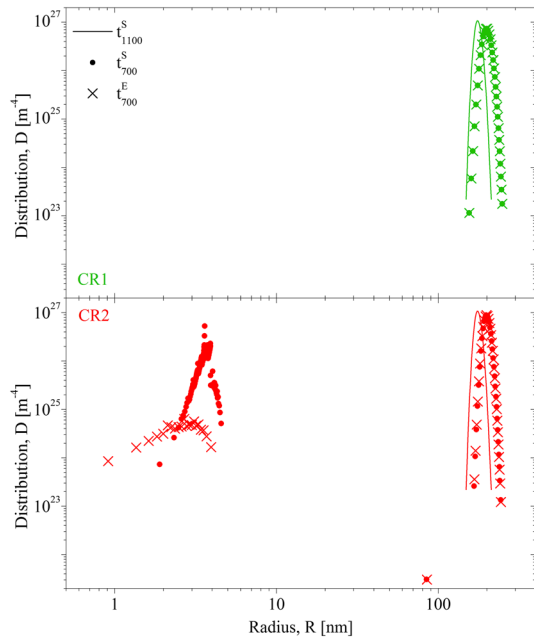


Fig. 12—Size distributions calculated for the two proposed heat treatments.

of 67.2 pct (CR1) and 66.9 pct (CR2) are already close to the equilibrium value (68.1 pct) when the 973 K (700 °C) temperature is met. The isothermal holding at 973 K (700 °C) has thus virtually no effect on the microstructure for CR1. This is visible in Figure 12, where no significant evolution of the size distribution is observed for CR1 between t_{700}^S and t_{700}^E . This situation can easily be explained by the fact that 973 K (700 °C) is a relatively low temperature for this category of alloys. For the CR2 heat treatment, the same observation applies to the first population of precipitates. However, the size distribution of the second populations broadens and shifts toward lower radii, which indicates dissolution of the small precipitates due to the coarsening. However, as for CR1, the quasi-totality of the volume fraction of γ' is made of the first population. The PSDs obtained with CR1 and CR2 are narrower than for the STD conditions. In the STD heat treatment, substantial coarsening takes place during the temperature plateaus at 1373 K and 1143 K (1100 °C and 870 °C), which causes a widening of the distribution.

The calculations indicate that shorter heat treatments, based on slow continuous cooling, could be used instead of classical aging heat treatments with temperature plateaus, still reaching similar particle radii and volume fractions. Narrower PSDs would also be expected. This analysis is based on the assumption that the local chemistry remains unchanged. In case of residual microsegregation, longer aging may be required to allow for long distance diffusion and further reduce the inhomogeneities in the material. Experimental work to characterize the microstructure and the mechanical properties would be required to confirm the benefits of continuous cooling heat treatments.

IV. CONCLUSIONS

A comprehensive modeling approach integrating solidification, homogenization, and aging has been applied to the industrial AM1 superalloy. Formation of γ' precipitates during aging was addressed with a model tracking the PSD. The model was coupled with thermodynamic equilibrium calculations to take into account the effects of high supersaturations and cross-diffusion, which are of great importance for application to multicomponent Ni-based alloys. The precipitation model was first validated through comparisons of the calculated average particle radius with experimental data collected on samples aged at 1373 K and 1483 K (1100 °C and 1210 °C). A good agreement was obtained without introducing any adjustable parameter in the simulation, beside a small adjustment of the γ/γ' interfacial energy within the range of values reported in the literature. This result indicates that classical homogeneous nucleation theory seems to be an adequate approach to simulate precipitation in AM1.

A multicomponent microsegregation model^[8,9] was used to generate the initial condition for aging and to perform chained microsegregation and precipitation calculations. The model was used to evaluate if a complete dissolution of γ' eutectic can be expected during the solution heat treatment. The results show that for the tested homogenization conditions, interdendritic γ' is expected to be still present in the microstructure, if relatively large dendrite arm spacing are considered (typically 100 μm or more). The calculations show a high sensitivity of the segregation level and residual interdendritic γ' with respect to the characteristic size of the microstructure, in both the as-cast and the homogenized states. It was shown that the homogenization rate of primary γ remains low as long as γ' is present in the microstructure. The complete dissolution of interdendritic γ' eutectic is thus found to be an important step in the solution heat treatment, in order to obtain uniform mechanical properties after aging.

The results of the chained solidification, homogenization, and aging simulations showed that residual segregation influences precipitation, in particular the volume fraction of the γ' precipitates. Similar nucleation, growth, and coarsening regimes were observed for the local compositions at the core and periphery of a dendrite arm. However, residual segregation affects substantially the local volume fraction of precipitates and their average radius, which can lead to inhomogeneities of the mechanical properties.

Finally, the precipitation model was used to investigate modified heat treatments consisting of slow continuous cooling rather than isothermal aging. Shorter heat treatments based on slow continuous cooling could be used to obtain similar particle radii and volume fractions as during the longer isothermal heat treatment. With continuous cooling, narrower PSDs are expected compared with isothermal aging, due to the nucleation of only one population of precipitate and lower amount of coarsening. Although these results remain to be confirmed by additional experiments and characterizations, they show the potential of the developed modeling

approach to explore new routes to optimize heat treatments.

ACKNOWLEDGMENT

The financial support of the Snecma-SAFRAN group is greatly acknowledged.

REFERENCES

1. R.C. Reed: *The Superalloys: Fundamentals and Applications*, Cambridge University Press, Cambridge UK, 2006.
2. J.A. Dantzig and M. Rappaz: *Solidification*, CRC Press, Taylor & Francis Group, Boca Raton, 2009.
3. C.E. Campbell, W.J. Boettinger, and U.R. Kattner: *Acta Mater.*, 2002, vol. 50, pp. 775–92.
4. N. Warnken, D. Ma, A. Drevermann, R.C. Reed, S.G. Fries, and I. Steinbach: *Acta Mater.*, 2009, vol. 57, pp. 5862–75.
5. N. Warnken: *J. Phase Equilib. Diffus.*, 2016, vol. 37, pp. 100–107.
6. C. Walter, B. Hallstedt, and N. Warnken: *Mater. Sci. Eng. A*, 2005, vol. 397, pp. 385–90.
7. Ch.-A. Gandin and A. Jacot: *Acta Mater.*, 2007, vol. 55, pp. 2539–53.
8. A. Jacot and M. Rappaz: *Acta Mater.*, 2002, vol. 50, pp. 1909–26.
9. Q. Du and A. Jacot: *Acta Mater.*, 2005, vol. 53, pp. 3479–93.
10. H. Combeau, J. Lacaze: *J. De Phys.*, 1993, vol. Iv 3, pp. 1157–62.
11. H.T. Pang, N. D'souza, N. Dong, H.J. Stone, and C.M.F. Rae: *Metall. Mater. Trans. A*, 2016, vol. 47A, pp. 889–906.
12. A. Szczotok and B. Chmiela: *J. Mater. Eng. Perform.*, 2014, vol. 23, pp. 2739–47.
13. F. Wang, D. Ma, S. Bogner, and A. Bührig-Polaczek: *Metall. Mater. Trans. A*, 2016, vol. 47A, pp. 2376–86.
14. J.S. Langer and A.J. Schwartz: *Phys. Rev. A*, 1980, vol. 21, pp. 948–58.
15. I.M. Lifshitz and V.V. Slyozov: *J. Phys. Chem. Solids*, 1961, vol. 19, pp. 35–50.
16. C. Wagner: *Zeitschrift für Elektrochemie*, 1961, vol. 65, pp. 581–91.
17. R. Kampmann and R. Wagner: in P. Haasen, V. Gerold, R. Wagner and F. Ashby Michael (Eds.): *Decomposition of Alloys: The Early Stages*. Pergamon Press, Sonnenberg, D, 1984, pp. 91–103.
18. M. Perez, M. Dumont, and D. Acevedo-Reyes: *Acta Mater.*, 2008, vol. 56, pp. 2119–32.
19. P. Maugis and M. Gouné: *Acta Mater.*, 2005, vol. 53, pp. 3359–67.
20. J. Svoboda, F.D. Fischer, P. Fratzl, and E. Kozeschnik: *Mater. Sci. Eng. A*, 2004, vol. 385, pp. 166–74.
21. E. Kozeschnik, J. Svoboda, P. Fratzl, and F.D. Fischer: *Mater. Sci. Eng. A*, 2004, vol. 385, pp. 157–65.
22. L. Rougier, A. Jacot, Ch.-A. Gandin, P. Di Napoli, P.-Y. Théry, D. Ponsen, and V. Jaquet: *Acta Mater.*, 2013, vol. 61, pp. 6396–6405.
23. L. Rougier, A. Jacot, Ch.-A. Gandin, D. Ponsen and V. Jaquet: *MATEC Web of Conferences*, 2014, vol. 14, 11003.
24. Q. Chen, J. Jeppsson, and J. Agren: *Acta Mater.*, 2008, vol. 56, pp. 1890–96.
25. C. Booth-Morrison, J. Weninger, C.K. Sudbrack, Z. Mao, R.D. Noebe, and D.N. Seidman: *Acta Mater.*, 2008, vol. 56, pp. 3422–38.
26. H. Aaron, D. Fainstein, and G. Kotler: *J. Appl. Phys.*, 1970, vol. 41, pp. 4404–10.
27. G. Guillemot and Ch.-A. Gandin: *Acta Mater.*, 2015, vol. 97, pp. 419–34.
28. Ch.-A. Gandin, Y. Bréchet, M. Rappaz, G. Canova, M. Ashby and H. Shercliff: *Acta Mater.*, 2002, vol. 50, pp. 901–27.
29. Ni20: Ni Base Alloys Database, Thermo-Calc Software AB, 2010.
30. MobNi2: *TCS Ni-alloys Mobility Database v2.0*, Thermo-Calc Software AB, 2011.
31. J.A. Marqusee and J. Ross: *J. Chem. Phys.*, 1984, vol. 80, pp. 536–43.
32. B.C. Wilson, E.R. Cutler, and G.E. Fuchs: *Mater. Sci. Eng. A*, 2008, vol. 479, pp. 356–64.
33. H. Ben Hamouda: *Modélisation et simulation de la structure de solidification dans les superalliages base-nickel: application AM1*, PhD Thesis, MINES ParisTech, Sophia-Antipolis, France, 2012.
34. A.L. Dons, L. Pedersen, and L. Arnberg: *Mater. Sci. Eng. A*, 1999, vol. 271, pp. 91–94.
35. C. Peyrourou and R. Tintiller: *Report « Précipitation et évolution de la phase gamma prime dans l'AM1: effet du temps et de la température »*, SNECMA, Gennevilliers, 1993.
36. X. Li, N. Saunders, and A. Miodownik: *Metall. Mater. Trans. A*, 2002, vol. 33A, pp. 3367–73.
37. T. Grosdidier, A. Hazotte, and A. Simon: *Mater. Sci. Eng. A*, 1998, vol. 256, pp. 183–96.
38. C. Mons: M1165, *Techniques de l'ingénieur*, Saint-Denis, France, (1996).
39. L. Rougier: *Simulation de la formation des microstructures dans les superalliages à base de nickel de type AM1 durant la solidification et les traitements thermiques*, PhD Thesis, EPFL, Switzerland (2013).